High-Resolution 3D Imaging and Quantification of Gold Nanoparticles in a Whole Cell Using Scanning Transmission Ion Microscopy

Xiao Chen,[†] Ce-Belle Chen,[†] Chammika N. B. Udalagama,[†] Minqin Ren,[†] Kah Ee Fong,[‡] Lin Yue Lanry Yung,[‡] Pastorin Giorgia,[§] Andrew Anthony Bettiol,[†] and Frank Watt[†*]

[†]Centre for Ion Beam Applications, Department of Physics, [‡]Department of Chemical and Biomolecular Engineering, and [§]Department of Pharmacy, National University of Singapore, Singapore

ABSTRACT Increasing interest in the use of nanoparticles (NPs) to elucidate the function of nanometer-sized assemblies of macromolecules and organelles within cells, and to develop biomedical applications such as drug delivery, labeling, diagnostic sensing, and heat treatment of cancer cells has prompted investigations into novel techniques that can image NPs within whole cells and tissue at high resolution. Using fast ions focused to nanodimensions, we show that gold NPs (AuNPs) inside whole cells can be imaged at high resolution, and the precise location of the particles and the number of particles can be quantified. High-resolution density information of the cell can be generated using scanning transmission ion microscopy, enhanced contrast for AuNPs can be achieved using forward scattering transmission ion microscopy, and depth information can be generated from elastically backscattered ions (Rutherford backscattering spectrometry). These techniques and associated instrumentation are at an early stage of technical development, but we believe there are no physical constraints that will prevent whole-cell three-dimensional imaging at <10 nm resolution.

INTRODUCTION

In the field of nanotechnology, especially for biomedical applications, scientists and clinicians are combining their efforts to enable medical intervention at the molecular scale for diagnosis, prevention, and treatment of diseases. Particles with submicroscopic dimensions represent ideal candidates for penetrating the least-accessible compartments within tissues and cells, and offer the additional advantage of escaping from premature degradation and elimination from the body.

Multifunctional nanoparticles (NPs) already have widespread biomedical applications (1,2), such as serving as carriers for targeted drug delivery and gene delivery (3), efficient contrast agents for molecular imaging in medical diagnostics (4), and therapeutic reagents for targeted photothermal therapy (5). Recently, NPs have proved to be useful in cancer therapy, allowing for effective and targeted drug delivery (6,7). However, because of the lack of adequate imaging techniques that can visualize three-dimensional (3D) local populations of NPs within a whole cell or inside cellular components (8), it remains difficult to investigate the mechanisms underlying a cell's ability to internalize external particles coupled with the transport of functionalized targeted NPs within the cell.

Single NPs cannot be resolved by conventional optical microscopy due to diffraction limits placed on its spatial resolution, and for that reason electron microscopy is typically used to visualize NPs. Although transmission electron microscopy (TEM) has been very successful at identifying NPs in thin cellular sections, it remains difficult to resolve gold NPs (AuNPs) at nanoscale resolution in the whole cell. Due to large-angle electron/electron scattering, electron microscopy can only maintain its high resolution in a thin sample, and therefore sample preparation for TEM typically includes processing of the samples into 50- to 200-nm-thin serial sections, a step that involves the risk of NP removal or displacement. A further disadvantage is the difficulty of obtaining quantitative results, since thin sections may slice through 3D structures such as vesicles containing high densities of NPs. To overcome these disadvantages, other techniques have been applied to image NPs inside whole cells. Scanning TEM (STEM) has been reported to have the ability to visualize AuNPs in a whole cell (9). This method involves scanning a focused beam of electrons over the sample layer by layer by changing the STEM focus so that a focal series of images with depth is recorded. STEM provides high-resolution imaging at ~10 nm in the focal plane. However, when the focal plane is located within the cell, the resolution is reduced due to electron scattering with atomic electrons in the sample, which results in a blurring of the image. By increasing the electron energy to several hundred kiloelectronvolts, one can reduce the electron scattering, but at the expense of a lower probability of electron interactions occurring within the sample. Another recently developed technique, known as scanning near-field ultrasonic holography, also offers a way to resolve subsurface NPs with <100 nm resolution (10,11).

Here we present a new, to our knowledge, approach to visualize AuNPs three-dimensionally and quantify the number of AuNPs within a whole cell. This technique, which is based on scanning transmission ion microscopy

Submitted November 6, 2012, and accepted for publication February 8, 2013.

*Correspondence: phywattf@nus.edu.sg

Editor: David Wolf.

0006-3495/13/04/1419/7 $2.00

http://dx.doi.org/10.1016/j.bpj.2013.02.015

(STIM), is similar to STEM except that heavier charged particles (ions) are used instead of electrons. Fast ions with sufficient energy to penetrate through a whole cell (e.g., >500 keV protons, and >1 MeV α particles) have great potential for imaging the internal structure of a cell because fast ions maintain a straight trajectory when traversing material. Fast ions interact with matter mainly through ion-electron collisions, and due to the high mass mismatch with electrons, ions suffer very low energy transfer and minimal scattering for each collision. As a result, thousands of collisions can occur before the ions stop, and the ion path is characterized by straight, deep penetration into the material (12). By detecting directly transmitted ions, one can obtain a map of energy loss contrast that includes detailed cell structural density information (STIM) (13).

In addition to ion-electron interactions, there is also a reduced probability that the MeV ion will undergo elastic scattering from atomic nuclei. The cross section for nuclear elastic collisions (σ) is well known and is given by

$$\sigma = \left[\frac{Z_1 Z_2 e^2}{4E_c \sin^2(\theta_c/2)}\right]^2 \quad (1)$$

where Z_1 and Z_2 are the atomic numbers of the incoming ion and the target ion, respectively; E_c is the incoming ion energy; and θ_c is the scattering angle from the original ion path.

In nuclear elastic collisions, the incoming ion can be forward scattered ($\theta_c < 90^\circ$) or backscattered ($\theta_c > 90^\circ$; Rutherford backscattering). By detecting forward-scattered ions at angles θ_c ~5–10°, one can obtain an image that reflects elemental information about the sample. In this technique, called forward STIM (FSTIM), the scattering cross section increases as Z^2 and therefore there is a higher probability of scattering from high-Z heavy elements compared with the low-mass elements (C, O, and H) normally found in the cell.

By measuring the energy of the backscattered ions (e.g., at θ_c ~160°), in a process known as Rutherford backscattering spectrometry (RBS), one can identify the depth position of the target atom, although at the expense of much lower scattering cross sections. RBS is a technique well known in materials research, and is particularly efficient for identifying elements and depth profiling heavy elements in low-mass matrices such as organic materials. In the case of AuNPs buried within a cell, the energy loss exhibited by backscattered ions is approximately proportional to the depth of the AuNP.

The current state-of-the-art performance for MeV ion beam focusing at the Centre for Ion Beam Applications, Department of Physics, National University of Singapore (14), is a 25 nm spot size for STIM and FSTIM at low probe currents of 5000–20,000 ions per second. This relatively low ion flux is due to the relatively low brightness of the radio-frequency ion source. The best spot sizes we have achieved for RBS are 200–300 nm. RBS relies on nuclear elastic scattering at backward angles, and because the scattering cross sections are low, the resolution is degraded because higher ion currents up to 100 pA are required.

Therefore, we employ three complementary and related techniques to obtain a 3D image of the NPs in the whole cell: 1), STIM (direct energy loss imaging using on-axis detection of transmitted ions to image cell structure); 2), FSTIM (detection of off-axis transmitted ions that have undergone forward nuclear scattering to provide a lateral image of the NPs in the cell); and 3), RBS (detection of backscattered ions to provide information about the depth of NPs in the cell).

MATERIALS AND METHODS

Synthesis and characterization of 100 nm AuNPs

The conventional Frens method (15) to synthesize large-size noble metal nanocrystals generally produces AuNPs with a wide size distribution. Therefore, to obtain AuNPs with better shape uniformity, we first prepared gold seeds by wet chemistry reduction, and then acquired the desired AuNPs by using a seed-mediated growth approach.

We prepared 10 nm gold seeds by reducing 0.01% of gold salt solution with 0.04% of citrate and 0.001% of tannic acid in a total volume of 20 mL at 70°C. When the reacting solution turned into clear crimson, the temperature was brought to 110°C, boiled for 5 min, and then cooled slowly in air to room temperature. These seeds were used to prepare 100 nm AuNPs according to a seeding-growth method adapted from Niu et al. (16) at room temperature. Briefly, a 50 mL reaction mixture containing 0.5 mM of $HAuCl_4$ and 98.4 μL of the synthesized 10 nm gold seeds was prepared in a conical flask so that the molar ratio of gold in solution to that in 10 nm gold seeds was fixed at 1000:1. After 5 min of vigorous stirring, 1.9 mL of 10 mM methane sulfonic acid (MSA), pH 7, was added quickly (molar ratio of gold in solution to MSA of 1:0.76). The reaction was allowed to proceed for 40 min under vigorous stirring. The solution gradually turned from faint yellow to reddish purple, indicating the formation of large-size AuNPs. Subsequently, the product was filtered and stored at 4°C until further use. TEM analysis showed that mean particle diameters for the gold seeds and the AuNPs were 10.03 ± 1.0 nm and 97.02 ± 5.1 nm, respectively. Both displayed size distributions within 10% of their respective mean diameters.

Coating of AuNPs

We passivated 100 nm AuNPs by incubating them in fetal bovine serum (FBS) at 37°C for 4 h. After removal of unbound FBS with phosphate-buffered saline (PBS) washes, FBS-coated AuNPs were concentrated by low-speed centrifugation (200 × g) to discourage aggregation. The concentration of the coated AuNPs was determined by spectrophotometric measurement and calculated using a molar extinction coefficient of 1.08×10^{11} $M^{-1}cm^{-1}$.

Cell sample preparation

HeLa cells were seeded on silicon nitride windows (100 nm thick) at a density of 6000 cells/cm^2 in Dulbecco's modified Eagle's medium (DMEM) supplemented with FBS (10%) and antibiotics penicillin (100 U/ml) and streptomycin (100 μg/ml). After attachment, control cells were rinsed with PBS and incubated in supplemented DMEM. The NP cells

were similarly incubated but also using FBS-coated 100 nm AuNPs (5 pM) for 24 h. Both control and NP cells were washed three times with pre-warmed PBS and fixed in glutaraldehyde (2.5%) for 24 h. The fixed cells were dehydrated with an ethanol gradient and then subjected to critical-point drying.

RESULTS AND DISCUSSION

A schematic diagram of the experimental setup is shown in Fig. 1. A focused beam of MeV ions passes through an annular surface barrier (RBS) detector and is scanned over the cell. The backscattered ions from the cell are detected by the RBS detector. The transmitted ions that are forward scattered at shallow angles are detected by an annular surface barrier (FSTIM) detector, and the ions that pass directly through the cell without significant angular scattering are detected by the STIM surface barrier detector.

Fig. 2 shows scanning electron microscopy (SEM) images of two cells: a HeLa cell grown in a control environment (control cell), and a HeLa cell grown in a 100 nm AuNP environment (AuNP cell). The AuNP cell image shows NPs present in the background, whereas in the control cell none are observed. Figs. 3 and 4 show STIM images of the control and AuNP cells at different magnifications. The images differ in that the SEM images depict the cell surface, whereas the STIM images depict the ion energy loss as the ions pass through the cell and thus are indicative of the internal structure of the cell. The STIM images show that the nuclei and nucleoli have greater densities compared with the surrounding cytoplasm and organelles, and although there is some evidence of nanosized structures in the AuNP cell images, the contrast is not sufficient to differentiate the AuNPs from other dense focal structures observed within the cell.

Fig. 5 shows images of the FSTIM results for both the control and AuNP cells. The FSTIM image of the AuNP cell, as expected, has increased scattering from the AuNPs. The contrast is high, and individual NPs as well as AuNP clusters are easily resolved. No AuNPs are detected in the control sample. The particles that are observed in the SEM image (Fig. 2 *b*), both in the background and on the cell surface, are either organic-inorganic nanostructures or AuNPs. However, the NPs that are visible in the FSTIM image (Fig. 5 *a*) are AuNPs only. In the FSTIM technique, the scattering cross section increases as Z^2 (see Eq. 1) and therefore there is a higher probability of scattering from high-Z heavy elements (e.g., gold) compared with, e.g., the carbon NPs. In the case of gold and carbon, because $Z_{gold} = 79$, and $Z_{carbon} = 6$, there is an enhancement of the ion scattering from gold by a factor of $(79)^2 / (6)^2 = 173$ times.

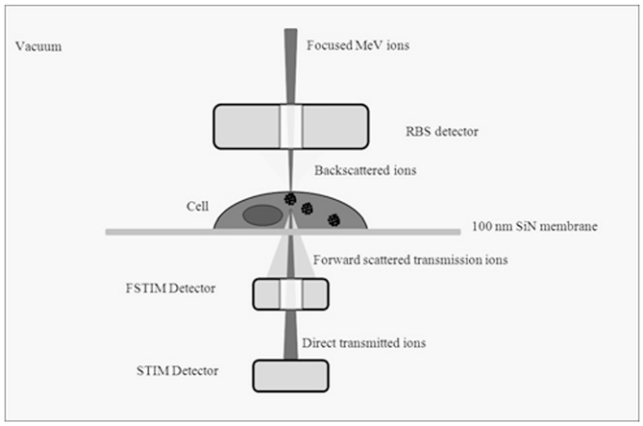

FIGURE 1 Schematic diagram of the experimental setup for cell imaging using fast ions.

FSTIM, however, does not differentiate between the AuNPs on the surface of the cell and those that have been internalized by the cell. Therefore, we need to utilize the depth-resolving feature of RBS to elucidate whether the particles are on the surface or within the cell. Fig. 6 shows the RBS energy spectrum from the cell scan and indicates the energy windows chosen to differentiate between surface and subsurface AuNPs. Images of the RBS results are shown in Fig. 7. The FSTIM image is shown in Fig. 7 *a* for comparison. Fig. 7 *b* shows the RBS image of the AuNPs obtained using the total RBS gold data and, as expected, is similar to Fig. 7 *a* except for the poorer spatial resolution exhibited by RBS. Fig. 7 *c* is the RBS image of the AuNPs obtained using only the backscattered ions from gold detected with low energy loss (i.e., from the surface), and Fig. 7 *d* shows the RBS image of the AuNPs obtained using only the backscattered ions from gold detected with high energy loss (i.e., the AuNPs from within the cell). These images clearly differentiate between the AuNPs that have been internalized by the cell (as in Fig. 7 *d*) and those that are still on the surface (Fig. 7 *c*). Further information can be obtained from the RBS results. For each AuNP or AuNP cluster, depth information can be extracted from the RBS data. Each AuNP or AuNP cluster can therefore be positioned within the cell: high-resolution (~25 nm) lateral information can be generated using FSTIM, and depth information can be generated from the RBS data. The energy resolution in our RBS detection system has been estimated at 24 keV, and if we use the typical stopping power of helium ions in a biological cell (192 KeV/um for 1.6 MeV helium ions) (17), we can estimate the depth resolution as 62 nm. A 3D image of the AuNPs within the cell can then be constructed. Fig. 8 shows the FSTIM image of the AuNP cell, using RBS depth information to color-code the depth of the AuNPs and AuNP clusters within the cell.

It can be seen from Fig. 7 *c* that, as expected, surface AuNPs are relatively evenly distributed on the cell substrate surface. However, consistent with the idea that AuNPs usually gain entry into cells through endocytosis and are enclosed in endosomal or lysosomal vesicles (18,19), the accumulation of intracellular AuNPs (as shown in Figs. 7 *d* and 8) is not uniform within the cell. The AuNPs appear

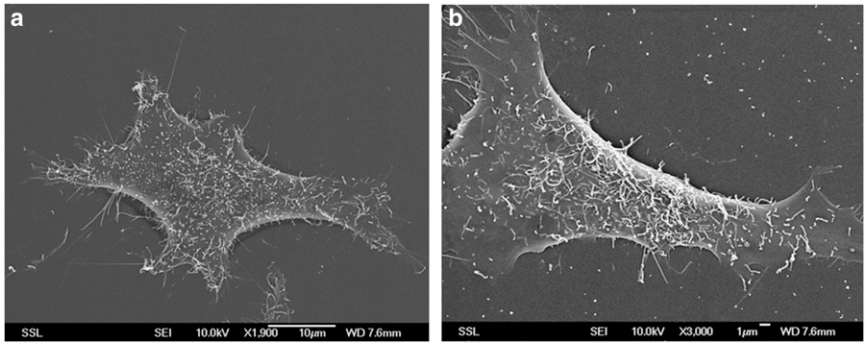

FIGURE 2 Scanning electron micrographs of (*a*) a HeLa cell (control) and (*b*) a HeLa cell cultured in an environment of AuNPs.

to coincide with the perinuclear region, which is the location of late endosomal or lysosomal compartments within the cell (20).

With regard to possible damage caused by the ion beam, the whole-cell STIM images are assembled using the method of pixel normalization. This is a technique in which the α beam is focused on a specific 25 nm $\times$ 25 nm pixel until a specific number of α particles (in this case 15) have been counted by the STIM detector positioned behind the cell (see Fig. 1). When 15 ions have been counted, the ion beam is then moved to the adjacent pixel, and in this way the scan can be rastered continuously over the sample. For one complete scan, the total ion flux through the cell is then 15 α particles for every 25 nm $\times$ 25 nm pixel over the area of the cell. The ion flux used to assemble the image (e.g., in Fig. 3, *a* and *b*) can then be assessed as 24,000 α particles/μm^2, or 0.024 α particles/nm^2. For STIM and FSTIM, we believe that at this low ion flux, the damage estimated in terms of any alteration of fine structure and displacement of atoms in the cell can be considered minimal, although this has to be confirmed.

Quantifying the number of NPs present within the cell

We can determine the number of AuNPs contained within the cell by using the RBS and FSTIM techniques.

Using RBS, the number of detected backscattered ions Y can be written as (21)

$$Y = \sigma \Omega Q Nt \quad (2)$$

where Q is the total number of incident particles, σ is the RBS cross section (from Eq. 1), and Ω is the detector solid angle, which can be measured from the detector geometry. By measuring Y, we can determine the number of atoms per unit area, Nt.

In the case of AuNPs in a biological cell, if we know the number of gold atoms present per unit area inside the cell, and we know the area of the cell, we can calculate the number of AuNPs corresponding to 100-nm-diameter gold spheres. Our RBS results indicate that 1256 AuNPs are located within the cell.

Using FSTIM, we can resolve individual NPs, and thus we can measure the number of forward scattered ions from a single NP. If we then measure the total number of forward scattered ions from all AuNPs within the cell (and we do not need to differentiate between single AuNPs and AuNP clusters), we can ascertain the total number of AuNPs. Using FSTIM, we measure 1341 AuNPs within the cell. The results are in good agreement and are within the experimental errors associated with each technique, estimated at ~10%. It should be noted that because we are considering nuclear scattering, any

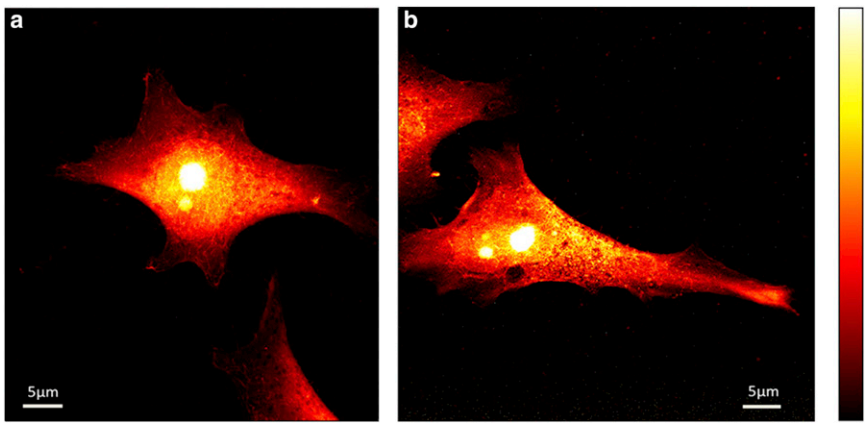

FIGURE 3 STIM images of (*a*) a HeLa cell (control) and (*b*) a HeLa cell cultured in an environment of AuNPs; 1.6 MeV helium ions.

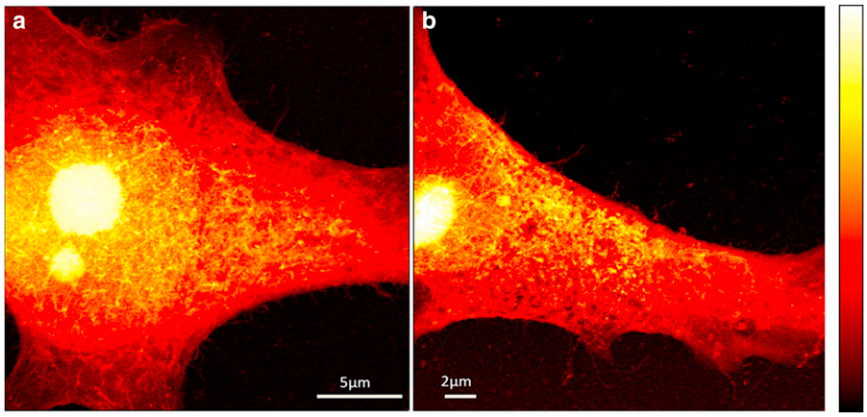

FIGURE 4 Higher-magnification STIM images of (*a*) a HeLa cell (control) and (*b*) a HeLa cell cultured in an environment of AuNPs; 1.6 MeV helium ions.

scattering due to chemical effects is negligible in both cases.

CONCLUSIONS

Using a beam of fast ions (in this case 1.6 MeV helium ions) focused to 25 nm, we can image AuNPs in a whole cell at lateral resolutions of ~25 nm, with an estimated depth resolution as derived from the RBS data of ~65 nm. Particles that have been assimilated into the cell can be resolved from particles residing on the surface, and using FSTIM and RBS we can ascertain the number of particles within the cell. The imaging times are relatively fast, with STIM and FSTIM taking ~15 min per cell, and RBS imaging taking ~1 h. It is worth mentioning that these techniques are not yet fully developed. With the development of new high-brightness ion sources in the near future, we expect to achieve spatial resolutions of <10 nm, as well as faster scanning times. We also emphasize that although STEM currently has superior focusing characteristics, the primary advantage of STIM lies in the virtual absence of angular scattering with atomic electrons in the sample. This single characteristic indicates that with further development, STIM will undoubtedly prove superior for 3D imaging of relatively thick samples such as whole cells.

The ability to form 3D high-resolution images will enable a quantitative evaluation of particle accumulation in specific cellular organelles and provide useful insights into the mechanism of internalization and the intracellular biodistribution of drugs (22). The cell internalization of AuNPs is influenced by both NP properties (e.g., size, shape, and surface (23,24)) and cell types or phases (25). By visualizing the accumulation of AuNPs (for example, in correspondence with lysosomes, which are organelles commonly involved in the digestion of molecules and particles derived from phagocytosis, endocytosis, and autophagy), we can obtain direct evidence of the mechanism involved and discriminate between an energy-mediated (i.e., active transport) or energy-independent cellular uptake of our NPs. The ability to quantify AuNPs in a whole cell is particularly useful for determining the efficacy of the internalization process for drug targeting and delivery, which is a critical goal in the development of medical uses for AuNPs. The idea is that AuNPs can act as a carrier because they can cross the cell membrane without disruption. The AuNPs can be functionalized to include target molecules on its surface to target specific parts of the cell (e.g., mitochondria, lysosomes, Golgi complex, and nucleus/nucleoli) as well as a fixed number of drug molecules for delivery when it reaches the target. Therefore, by measuring the

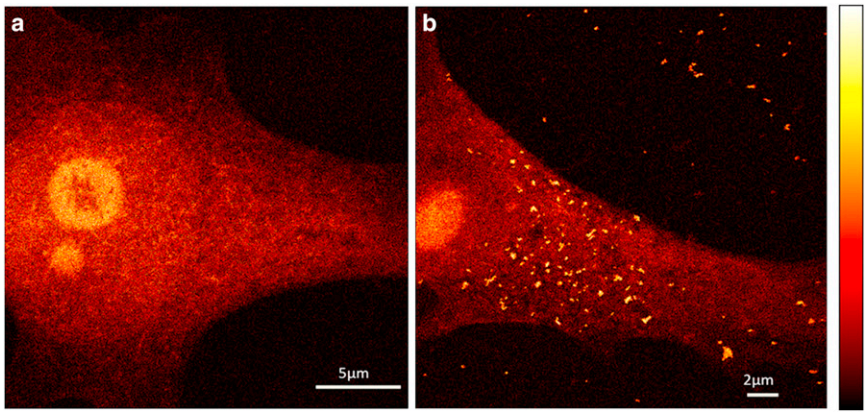

FIGURE 5 FSTIM images of (*a*) a HeLa cell (control) and (*b*) a HeLa cell cultured in an environment of AuNPs; 1.6 MeV helium ions.

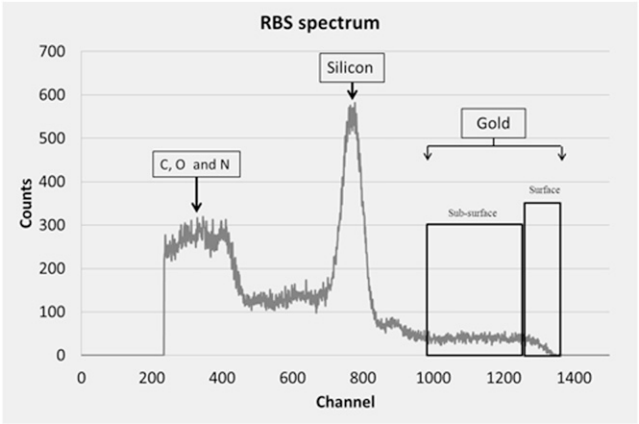

FIGURE 6 RBS energy spectrum from the NP cell, showing C and O counts from the cell, Si and N counts from the silicon nitride window, and Au counts from the NPs; 1.6 MeV helium ions.

number and distribution of the AuNPs, we will be able to ascertain how effective the drug delivery is in terms of distribution and dose. We also have to recognize that excessive use of AuNPs for therapeutic purposes may induce potential toxicity in the cell. It seems likely that beyond a critical threshold of NP uptake, free-radical damage is more likely to be induced within the cell. Therefore, it is important to monitor NP uptake in conjunction with free-radical damage, although for cancer treatment this is not a problem because the goal is to critically damage the cell.

We are also developing the use of MeV protons for 3D structural identification of AuNPs. The use of protons will

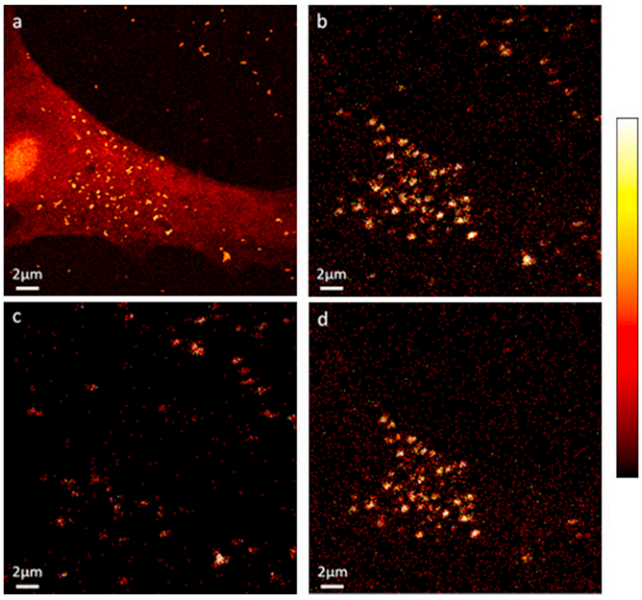

FIGURE 7 (*a*) FSTIM image of a HeLa cell cultured in an environment of AuNPs. (*b*) Total RBS Au image of a HeLa cell cultured in an environment of AuNPs. (*c*) Surface RBS Au image of a HeLa cell cultured in an environment of AuNPs. (*d*) Subsurface RBS Au image of a HeLa cell cultured in an environment of AuNPs.

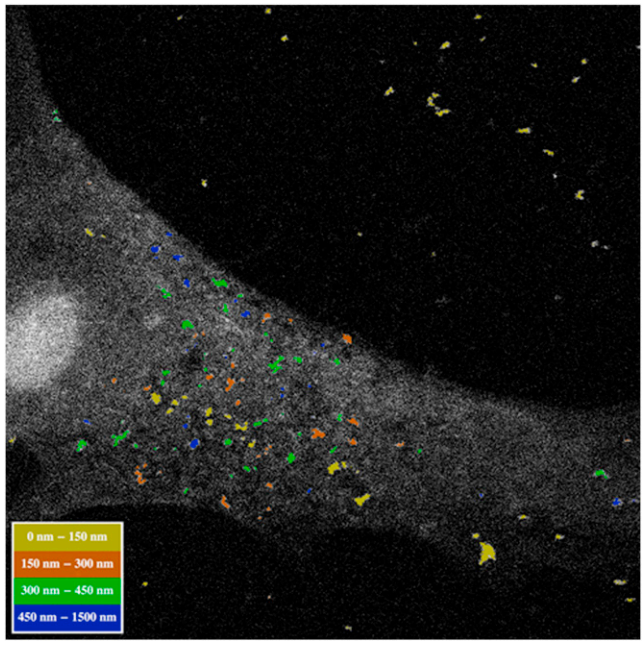

FIGURE 8 FSTIM image of the NP cell, using RBS depth information to color code the depth of the NPs and NP clusters within the cell; 0–150 nm represents the surface NPs.

also allow proton-induced fluorescence (PIF) imaging to be carried out simultaneously at high resolutions. Because the secondary electrons generated by the primary proton beam have low energy and therefore a short range (<5 nm), the fluorescence generated by the secondary electrons remains localized around the proton beam trajectory. Therefore, <10 nm fluorescence imaging is feasible, and by using targeted fluorescent cell markers, one can locate the organelles and identify the specific location of the AuNPs with respect to those organelles. The combination of STIM, FSTIM, RBS, and PIF has great potential for elucidating the dynamics and interaction of AuNPs within whole cells.

We wish to acknowledge the Faculty of Science, National University of Singapore (MOE tier 1 research grant R-148-000-164-112 and research grant R-398-000-068-112).

REFERENCES

1. Petros, R. A., and J. M. DeSimone. 2010. Strategies in the design of nanoparticles for therapeutic applications. *Nat. Rev. Drug Discov.* 9:615–627.
2. Sperling, R. A., P. Rivera Gil, …, W. J. Parak. 2008. Biological applications of gold nanoparticles. *Chem. Soc. Rev.* 37:1896–1908.
3. Ghosh, P., G. Han, …, V. M. Rotello. 2008. Gold nanoparticles in delivery applications. *Adv. Drug Deliv. Rev.* 60:1307–1315.
4. Weissleder, R., and M. J. Pittet. 2008. Imaging in the era of molecular oncology. *Nature.* 452:580–589.
5. Lal, S., S. E. Clare, and N. J. Halas. 2008. Nanoshell-enabled photothermal cancer therapy: impending clinical impact. *Acc. Chem. Res.* 41:1842–1851.

6. Cho, K., X. Wang, …, D. M. Shin. 2008. Therapeutic nanoparticles for drug delivery in cancer. *Clin. Cancer Res.* 14:1310–1316.
7. Farokhzad, O. C., J. Cheng, …, R. Langer. 2006. Targeted nanoparticle-aptamer bioconjugates for cancer chemotherapy in vivo. *Proc. Natl. Acad. Sci. USA.* 103:6315–6320.
8. Stone, V., and K. Donaldson. 2006. Nanotoxicology: signs of stress. *Nat. Nanotechnol.* 1:23–24.
9. Peckys, D. B., and N. de Jonge. 2011. Visualizing gold nanoparticle uptake in live cells with liquid scanning transmission electron microscopy. *Nano Lett.* 11:1733–1738.
10. Tetard, L., A. Passian, …, T. Thundat. 2008. Imaging nanoparticles in cells by nanomechanical holography. *Nat. Nanotechnol.* 3:501–505.
11. Shekhawat, G. S., and V. P. Dravid. 2005. Nanoscale imaging of buried structures via scanning near-field ultrasound holography. *Science.* 310:89–92.
12. Udalagama, C., A. A. Bettiol, and F. Watt. 2009. Stochastic spatial energy deposition profiles for MeV protons and keV electrons. *Phys. Rev. B.* 80:224107.
13. Chen, X., C. N. Udalagama, …, F. Watt. 2011. Whole-cell imaging at nanometer resolutions using fast and slow focused helium ions. *Biophys. J.* 101:1788–1793.
14. Watt, F., X. Chen, …, A. A. Bettiol. 2011. The Singapore high resolution single cell imaging facility. *Nucl. Instrum. Methods Phys. Res. B.* 269:2168–2174.
15. Frens, G. 1973. Controlled nucleation for the regulation of the particle size in monodisperse gold suspensions. *Nat. Phys.* 241:20–22.
16. Niu, J., T. Zhu, and Z. Liu. 2007. One-step seed-mediated growth of 30–150 nm quasispherical gold nanoparticles with 2-mercaptosuccinic acid as a new reducing agent. *Nanotechnology.* 18:325607.
17. Biersack, J. F. Z. J. P. http://www.srim.org.
18. Iversen, T.-G., T. Skotland, and K. Sandvig. 2011. Endocytosis and intracellular transport of nanoparticles: present knowledge and need for future studies. *Nano Today.* 6:176–185.
19. Lévy, R., U. Shaheen, Y. Cesbron, and V. Sée. 2010. Gold nanoparticles delivery in mammalian live cells: a critical review. *Nano Rev.* 1:3402.
20. Hao, X., J. Wu, …, H. Wang. 2012. Caveolae-mediated endocytosis of biocompatible gold nanoparticles in living Hela cells. *J. Phys. Condens. Matter.* 24:164207.
21. Chu, W.-K. 1978. Backscattering Spectrometry. Academic Press, New York.
22. Khlebtsov, N., and L. Dykman. 2011. Biodistribution and toxicity of engineered gold nanoparticles: a review of in vitro and in vivo studies. *Chem. Soc. Rev.* 40:1647–1671.
23. Lundqvist, M., J. Stigler, …, K. A. Dawson. 2008. Nanoparticle size and surface properties determine the protein corona with possible implications for biological impacts. *Proc. Natl. Acad. Sci. USA.* 105:14265–14270.
24. Chithrani, B. D., A. A. Ghazani, and W. C. W. Chan. 2006. Determining the size and shape dependence of gold nanoparticle uptake into mammalian cells. *Nano Lett.* 6:662–668.
25. Kim, J. A., C. Åberg, …, K. A. Dawson. 2012. Role of cell cycle on the cellular uptake and dilution of nanoparticles in a cell population. *Nat. Nanotechnol.* 7:62–68.